Dark ice chemistry in interstellar clouds

Qasim, D.N.

Methanol ice formation threshold in dense clouds and dark cores revisited

CH_3OH is a central molecule for interstellar complex organic molecule formation. Theoretical, experimental, and observational studies have shown that it is formed abundantly by the hydrogenation of CO-rich ice, deep inside cold, dark cores (formation threshold of $A_V > 9$ mag). This scenario does not seem uniformly applicable, however, because observations have shown a deficiency of the CH_3OH ice abundance, by at least a factor of 3, in a significant number of dark core and dense cloud sight-lines tracing depths well above 9 mag. Also, at shallower depths, CH_3OH may still be formed, but at lower abundances, via, e.g., CH_4 abstraction reactions (Qasim et al. 2018).

In this study, we aim to help address these questions by re-analyzing previously published data (Boogert et al. 2011), as well as new L−band spectra of a sample of dense cloud and dark core sight-lines toward background stars. Focus was put into increasing the sensitivity to CH_3OH abundances, enabling an improved study of abundance variations as a function of cloud/core depth. The detection and absorption profile analysis of weak ice features in dense clouds and dark cores, such as those of CH_3OH, are limited by the contamination with photospheric absorption lines of the background stars. We demonstrate a method to reduce photospheric contamination by dividing over the spectra of un-reddened stars from the NASA Infrared Telescope Facility database.

In a sample of 41 stars behind quiescent dense cloud material and isolated dense cores we report 1 new CH_3OH ice detection, bringing the total to 8. The CH_3OH ice abundances are 3.4-21% relative to H_2O, corresponding to 1.6×10^{-6} – 8.8×10^{-6} relative to H_2. A linear fit to these detections yields a CH_3OH ice detection threshold of only 13.5 ± 7.8 mag. This is within the uncertainty range from Boogert et al. (2011).

Significant non-detections are reported in 34 sight-lines. After correction for the photospheric lines, and at sufficiently high S/N, the CH_3OH ice abundances are limited by the contamination with the 3.47 μm ice feature (likely due to $NH_3.H_2O$ hydrates). Still, the CH_3OH ice abundance upper limits (rel-

D. Qasim, A.C.A. Boogert, D. Harsono, J.V. Keane, and H. Linnartz, *The methanol ice formation threshold in dense clouds and dark cores revisited*, in preparation

ative to A_V and H_2O) are low across the entire observed detection threshold A_V range of 5.1–46.0 mag: <0.34% relative to H_2O at A_V = 5.1-16.8 mag, and <0.21% relative to H_2O at A_V = 19.6-46.0 mag.

These results put strict observational constraints on the formation efficiency of CH_3OH ice. A full understanding requires the measurement of the CO ice abundance, as well as ice maps to trace the CO freeze out and CH_3OH formation rate in individual clouds and cores. This will be possible with the upcoming James Webb Space Telescope (JWST). Our method of the photospheric line correction of background star spectra can be applied to the JWST observations.

5.1 Introduction

Grain surface ice chemistry is initiated in the translucent phase of interstellar clouds (density of $\sim 10^3$ H_2 molecules cm^{-3}), and is further accelerated at densities of $\sim 10^4$ - 10^5 cm^{-3} in dense clouds and dark cores (Pontoppidan 2006; Boogert et al. 2015). At a cloud depth corresponding to a visual extinction (A_V) of $\sim$ 1.6 mag, a H_2O-rich ice is present, in which the ice matrix is composed of simple species such as NH_3, CO_2, and CH_4 (Boogert et al. 2015). At $\sim$ 3 mag, some CO ice grows to form an apolar layer (Chiar et al. 1995). At greater depths of $A_V \sim 9$ mag (10^5 cm^{-3}), CO freezes out nearly completely (Jørgensen et al. 2005; Pontoppidan 2006; Boogert et al. 2015), and is hydrogenated to form methanol (CH_3OH), as confirmed by a number of laboratory, modeling, and observational studies (Watanabe & Kouchi 2002; Fuchs et al. 2009; Cuppen et al. 2009; Boogert et al. 2011; Wirström et al. 2011). A list of the physical parameters of translucent, dense clouds, and dark cores is provided in Table 5.1.

Table 5.1: Physical conditions of the different regions of interstellar clouds, as noted in Table II of van Dishoeck et al. (1993). (a) Dust temperatures are much lower for all noted regions.

ISM region	Density (cm^{-3})	Gas temperature[a] (K)	A_V (mag)
Translucent	500-5000	15-50	1-5
Dense cloud	10^2 - 10^4	$\gtrsim$ 10	$\gtrsim$2
Cold, dark core	10^4 - 10^5	$\approx$ 10	5-25

Hydrogen addition and abstractions reactions in the pathway to CH_3OH also lead to an assortment of complex organic molecules (COMs), such as glycolaldehyde, ethylene glycol, and methyl formate (Chuang et al. 2016), in addition to glycerol (Fedoseev et al. 2017), propanal and 1-propanol (Qasim et al. 2019b). During the dispersal of the envelopes of the Young Stellar Objects (YSOs), the temperature rises, which increases the mobility of ice species and molecular complexity (e.g., Herbst & van Dishoeck 2009). At reduced dust extinctions, enhanced UV-irradiation of CH_3OH ice leads to various COMs as well (Öberg et al. 2009). COMs formed in the ice are released into the gas-phase, however COMs may also be formed in the gas-phase starting from simple molecules that were liberated from the ice (Charnley et al. 1992). Low abundances of

gas phase COMs are also detected in cold (T = 10 K) molecular clouds, where CH_3OH ice is a likely precursor (Soma et al. 2018).

CH_3OH is a key interstellar molecule to complex chemistry, so understanding its prevalence and formation conditions are important. Observations have not provided a consistent formation model. At similar A_V, the CH_3OH ice abundance relative to H_2O varies between detections of 10% and 3σ upper limits of 3% (Boogert et al. 2011, 2015). Perhaps the CO freeze out is limited in certain clouds and cores. For background star observations of dense clouds, a sight-line with a high A_V may have a long pathlength at low density. Lower densities result in higher dust temperatures, which would then decrease the freeze-out and hydrogenation rates of CO (Cuppen et al. 2009). However, this lack of CH_3OH at high A_V has been observed in numerous dark cores (Boogert et al. 2011), and dark cores have high A_V and high densities. Alternatively, CO may be consumed into other reactions, as also proposed in Shimonishi et al. (2016). The CO hydrogenation chain includes many other products besides CH_3OH, as illustrated in Figure 1 of Fedoseev et al. (2017). The low CH_3OH abundance deep in some clouds and cores could also be due to destruction either by internal UV-photons (Öberg et al. 2009) and/or H-abstraction reactions (Goumans & Kästner 2011; Chuang et al. 2016). On the other hand, CH_3OH formation should not be limited to the formation threshold of ~ 9 mag (Boogert et al. 2015), as other formation routes should be relevant at shallower cloud depths. For example, in the laboratory investigation by Qasim et al. (2018), it was found that the CH_4 + OH formation route to CH_3OH should proceed on grain mantles, although at a factor of 20 lower efficiency compared to H addition in CO ices. CH_4 is formed at low extinctions, and there is tentative observational evidence that it is enhanced at cloud edges where not all C has been included in CO yet (Öberg et al. 2008).

Observational constraints on CH_3OH formation models are only based on a handful of detections in dark cores (with and without embedded YSOs) (Boogert et al. 2011; Chiar et al. 2011; Pontoppidan et al. 2003). This limited sample size is in part due to the low sensitivity that is available from current observational facilities, as well as the lack of ice mapping capabilities. The James Webb Space Telescope (JWST), which is expected to be launched in 2021, will significantly improve on both aspects.

Ices in dense clouds and dark cores are typically observed in spectra of background field stars, which are typically cool stars (K- and M-giants). The detection of the ice bands, as well as their absorption profile analysis, is often limited by photospheric line contamination. Here, we present a method to increase the sensitivity of previously published and new observations of the C-H symmetric stretching mode of CH_3OH ice at 3.537 μm by dividing out photospheric lines using spectra of un-reddened stars from the NASA Infrared Telescope Facility (IRTF) database (Rayner et al. 2009). Section 5.2 overviews the parameters of the dust/ice observations and data reduction. All observations were taken towards *background stars*. Section 5.3 details the steps involved in reducing the photospheric lines and measuring the CH_3OH column densities. Sections 5.4 and 5.5 show the application of the method to increase the sensitivity of the data and accuracy of the data analysis in order to better constrain the formation parameters of CH_3OH. Section 5.6 outlines the main findings and proposed work for future studies.

5.2 Observations and data reduction

41 different background stars were observed in the atmospheric L−band with the NASA IRTF/SpeX (Rayner et al. 2003) and Keck 2/NIRSPEC (McLean et al. 1998) spectrometers, tracing the quiescent material in 12 different dense clouds and isolated dense cores (Table 5.2). Some cores contain embedded YSOs, and it is also not certain whether the dense cloud sight-lines trace high densities ($\sim 10^4$), or low densities in long pathlengths. Note that some targets were observed with both SpeX and NIRSPEC. The targets were selected to trace molecular material at a wide range of detection threshold extinctions A_V= 5.1-48.0 mag, as determined from model fits to 1-5 μm broad-band photometry and spectroscopy (Boogert et al. 2011, and in preparation). The spectra of 25 targets were previously published in Boogert et al. (2011).

Table 5.2 also lists the observational parameters, including the spectrometer used, wavelength range covered, the standard star used to reduce telluric contamination, the date of the observation, and the signal-to-noise (S/N) of the continuum emission near the wavelength of the CH_3OH ice band at 3.537 μm (3.460 - 3.530 μm; a region with relatively few telluric lines).

The SpeX instrument was used in the LongXD(1.9) mode, with a slit width of 0.8 arcseconds, resulting in a resolving power $R = \lambda/\Delta\lambda$ = 938. Data reduction was performed using the software package SpeXtool (Cushing et al. 2004) and Xtellcor (Vacca et al. 2003). Keck/NIRSPEC was used in the long-slit mode with a slit width of 0.57 arcseconds, resulting in a resolving power of ~1600. The data reduction procedure for these observations is discussed in Boogert et al. (2011). The wavelength calibration for both SpeX and NIRSPEC is based on telluric emission lines. The radial velocity of the targets was not corrected for.

5.3 Photospheric line correction and column determination

A Python script was created to reduce contamination by photospheric absorption lines from the interstellar dust and ice spectra by fitting un-reddened template spectra from the IRTF spectral library (Rayner et al. 2009). The best-fitting templates for each source, ${\chi_\nu}^2$ (reduced-χ^2), and the CH_3OH column densities derived from the photosphere-corrected spectra are presented in Table 5.3. The following steps were used in this procedure:

1) The spectral resolution of the template spectra (R = 2500 in the L−band; slit width of 0.3 arcseconds) was matched to those of the observed spectra by applying boxcar smoothing. Typically, a boxcar value of 3 was found to be sufficient for the lower resolution SpeX spectra, and no smoothing was needed for the NIRSPEC spectra.

2) A cross-correlation was applied to detect differences of the central wavelengths of the photospheric lines between the template and background star spectra. A wavelength shift was subsequently applied to the science spectrum, correcting for small wavelength calibration errors as well as differences in the radial velocity. In the wavelength range relevant for this work (~3.34-3.71 μm), shifts of < 70 km/s were typically applied, but sometimes as large as 170 km/s.

Table 5.2: Observational parameters. Extinction A_V calculated assuming $A_V/A_K = 8$ (Cardelli et al. 1989). B2011: published in Boogert et al. (2011).

Source 2MASS J	Cloud/Core	Instrument	λ μm	Standard star (SPT)	Date	Continuum S/N yyyy/mm/dd	Notes 3.537μm
04215402+1530299	IRAM 04191	NIRSPEC	2.82-4.14	HR 1251 (A0.5V)	2006/10/09	45	B2011
17111501-2726180	B 59	NIRSPEC	2.41-4.14	HR 6141 (B3V)	2005/06/28	54	B2011
17111538-2727144	B 59	NIRSPEC	2.41-4.14	HR 6141 (B3V)	2005/06/28	55	B2011
17112005-2727131	B 59	NIRSPEC	2.38-4.14	HR 5993 (B1V)	2006/07/07	52	B2011
17155573-2055312	L 100	NIRSPEC	2.38-4.14	HR 5993 (B1V)	2006/07/06	54	B2011
17160467-2057072	L 100	NIRSPEC	2.39-4.14	HR 6946 (B2II)	2005/06/29	41	B2011
17160860-2058142	L 100	NIRSPEC	2.38-4.14	HR 5993 (B1V)	2006/07/06	76	B2011
18140712-0708413	L 438	NIRSPEC	2.82-4.14	HR 7141 (A5V)	2006/10/09	79	B2011
18160600-0225539	CB 130-3	NIRSPEC	2.82-4.14	HR 7141 (A5V)	2006/10/09	65	B2011
18165296-1801287	L 328	NIRSPEC	2.41-4.14	HR 6946 (B2II)	2005/06/28	64	B2011
18165917-1801158	L 328	NIRSPEC	2.41-4.14	HR 6946 (B2II)	2005/06/28	50	B2011
18170376-0815070	L 429-C	NIRSPEC	3.00-3.87	HR 6963 (B9V)	2018/06/01	43	
18170426-1802408	L 328	NIRSPEC	2.06-4.14	HR 6946 (B2II)	2005/06/29	52	B2011
18170429-1802540	L 328	NIRSPEC	2.39-4.09	HR 6946 (B2II)	2005/06/29	56	B2011
18170470-0814495	L 429-C	NIRSPEC	2.38-4.14	HR 7141 (A5V)	2006/07/07	62	B2011
18170957-0814136	L 429-C	NIRSPEC	2.38-4.14	HR 7141 (A5V)	2006/07/07	63	B2011
18171181-0814012	L 429-C	NIRSPEC	2.06-4.14	HR 7141 (A5V)	2006/10/09	43	B2011
18171366-0813188	L 429-C	NIRSPEC	2.06-4.14	HR 7141 (A5V)	2006/10/09	39	B2011
18171700-0813504	L 429-C	NIRSPEC	3.00-3.87	HR 6963 (B9V)	2018/06/01	54	
18172690-0438406	L 483	NIRSPEC	2.38-4.14	HR 7141 (A5V)	2006/10/09	59	B2011
18275901+0002337	Serpens MC	IRTF	1.92-4.19	HR 7141 (A5V)	2010/05/22	50	
		NIRSPEC	2.77-4.23	HR 7141 (A5V)	2009/10/12	62	
18282010+0029141	Serpens MC	IRTF	1.92-4.19	HR 7141 (A5V)	2010/05/24	28	
		NIRSPEC	2.77-4.23	HR 6744 (A5E)	2009/10/12	37	
18282631+0052133	Serpens MC	IRTF	1.92-4.19	HD 163336 (A0V)	2010/05/20	89	
		NIRSPEC	2.77-4.23	HR 7141 (A5V)	2009/10/12	116	
18284038+0044503	Serpens MC	IRTF	1.92-4.19	HD 161868 (A1V)	2010/05/21	34	
		NIRSPEC	2.77-4.23	HR 7141 (A5V)	2009/10/12	49	
18284797+0037431	Serpens MC	IRTF	1.92-4.19	HR 7141 (A5V)	2010/05/24	32	
		NIRSPEC	2.77-4.23	HR 7141 (A5V)	2009/10/12	50	
18285266+0028242	Serpens MC	NIRSPEC	2.75-4.21	HR 7141 (A5V)	2007/07/05	31	
18290316+0023090	Serpens MC	IRTF	1.92-4.19	HD 161868 (A1V)	2010/05/2	34	
		NIRSPEC	2.77-4.23	HR 7141 (A5V)	2009/10/12	63	
18290436+0116207	Serpens MC	IRTF	1.92-4.19	HR 7141 (A5V)	2010/05/20	41	
		NIRSPEC	2.77-4.23	HR 7141 (A5V)	2009/10/12	71	
18291619+0045143	Serpens MC	NIRSPEC	2.77-4.23	HR 7141 (A5V)	2009/10/12	55	
18291699+0037191	Serpens MC	IRTF	1.92-4.19	HR 6629 (A1V)	2010/05/23	19	
		NIRSPEC	2.77-4.23	HR 7141 (A5V)	2009/10/12	41	
18292528+0003141	Serpens MC	IRTF	1.92-4.19	HR 7141 (A5V)	2010/05/20	53	
		NIRSPEC	2.77-4.23	HR 7141 (A5V)	2009/10/12	62	
18294108+0127449	Serpens MC	IRTF	1.92-4.19	HR 7141 (A5V)	2010/05/23	26	
		NIRSPEC	2.77-4.22	HR 7141 (A5V)	2009/10/12	72	
18300061+0115201	Serpens MC	IRTF	1.92-4.19	HR 6744 (A0V)	2010/05/22	41	
		NIRSPEC	2.77-4.23	HR 7141 (A5V)	2011/04/18	47	
		NIRSPEC	2.82-4.14	HR 7141 (A5V)	2009/10/12	47	B2011
18300085+0017069	Serpens MC	IRTF	1.92-4.19	HR 7141 (A5V)	2010/05/23	110	
		NIRSPEC	2.77-4.23	HR 7141 (A5V)	2009/10/12	51	
18300896+0114441	Serpens MC	IRTF	1.92-4.19	HD 163336 (A0V)	2010/05/22	38	
		NIRSPEC	2.77-4.22	HR 7141 (A5V)	2009/10/12	64	
19201597+1135146	CB 188	NIRSPEC	2.41-4.14	HR 7724 (A1V)	2005/09/20	54	B2011
19201622+1136292	CB 188	NIRSPEC	2.06-4.14	HR 7724 (A1V)	2005/09/20	56	B2011
19214480+1121203	L 673-7	NIRSPEC	2.06-4.14	HR 7141 (A5V)	2006/07/07	62	B2011
21240517+4959100	L 1014	NIRSPEC	1.49-4.14	HR 7929 (B2V)	2005/06/28	65	B2011
21240614+4958310	L 1014	NIRSPEC	1.49-4.14	HR 7929 (B2V)	2005/06/28	72	B2011
22063773+5904520	L 1165	NIRSPEC	1.49-4.14	HR 8585 (A1V)	2006/10/09	117	B2011

3) After interpolating the modified template spectrum to the source spectrum, the source spectrum was divided by the template to produce a "residual" spectrum.

4) The "residual" spectrum was divided by a smooth baseline, constructed by applying a Savitzky-Golay filter. Subsequently, the standard deviation was measured in the range of 3.6 - 4.0 μm (i.e., the range at which photospheric lines are strongly present, and telluric and ice features are relatively weak).

The best-fitting template was selected to be the one resulting in the lowest standard deviation in the "residual" spectrum divided by a smooth baseline. Also, a range of best-fitting spectral types was determined by selecting those with χ^2_ν values within a factor of 2 of the minimum, although a precise spectral classification of the background stars is not the primary goal of this work.

After the division of the observed background star spectrum over the best fitting template spectrum, the ice features were analyzed. The well known 3.47 μm ice absorption feature, which overlaps with the 3.53 μm CH_3OH ice feature, is readily visible in many spectra. The 3.47 μm absorption feature is usually attributed to the ν(O–H···N) mode of ammonia hydrates, $NH_3{\cdot}H_2O$ (Dartois & d'Hendecourt 2001), although this is still open to interpretation (Shimonishi et al. 2016). A second or third order polynomial was fitted to the continuum surrounding this feature, in the wavelength ranges 3.34-3.36 and 3.60-3.70 μm (see Appendix 5.7).The photospheric line-corrected background star spectrum F was converted into optical depth (τ) scale using this baseline F_0 as follows:

$$\tau = -\ln(F/F_0) \tag{13}$$

Subsequently, two gaussians were fitted simultanesously to the overlapping 3.537 μm and 3.47 μm features. This decomposition method is similar to what was used for YSO spectra in Brooke et al. (1999). Instead of using a laboratory spectrum of CH_3OH, we applied a gaussian with a similar peak position and width (FWHM) as the main peak of the CH_3OH laboratory spectrum: 3.537 and 0.04 μm, respectively. For the second gaussian, we used values of 3.47 and 0.1 μm. The fitting procedure was performed in Python, using the GaussianModel class within the package, LmFit. An example of the decomposition of the two peaks is shown in Figure 5.1.

The CH_3OH column, $N(CH_3OH)$, was then derived following

$$N(CH_3OH) = \frac{\tau_0 \times FWHM}{A} \tag{14}$$

where the full width at half maximum (FWHM) was fixed at 32 cm^{-1} (0.04 μm) and the peak optical depth (τ_0) was derived with the Gaussian fits. The integrated band strength (A) of 5.6×10^{-18} cm molecule $^{-1}$ for the C-H symmetric stretching mode of solid CH_3OH was obtained from Kerkhof et al. (1999).

5.4 Results

The CH_3OH ice column densities and 3σ upper limits are presented in Table 5.3, along with the best-fitting templates for each source spectrum and

Table 5.3: CH_3OH column densities in cm^{-2} and relative to H_2O ice for all observed dense cloud and dark core lines of sight after correction for the photospheric absorption lines. The upper limits have 3σ significance and are indicated by (<). The uncertainties of the detections are 1σ and are indicated by parentheses. The uncertainty range for the spectral types is based on the template stars that have χ^2_ν values within a factor 2 of the minimum. A_V and the H_2O column densities are obtained from Boogert et al. (2011) and Boogert et al. (in preparation). (*) indicates CH_3OH detected in this sight-line in Boogert et al. (2011). B2011: published in Boogert et al. (2011).

Source	Instrument	A_V	Template star[1]	χ_ν^2	$N(H_2O)$	$N(CH_3OH)$		Notes
2MASS J			mag		10^{18} cm^{-2}	10^{17} cm^{-2}	$\%H_2O$	
04215402+1530299	NIRSPEC	24.3	HD6903/F9 (F5-G2)	0.0021	1.84 (0.20)	<0.097	<0.53	B2011
17111501-2726180	NIRSPEC	31.3	HD94705/M5.5 (M0-M5)	0.00051	2.35 (0.26)	<0.084	<0.36	B2011
17111538-2727144	NIRSPEC	28.2	HD120052/M2 (M0-M3)	0.0018	2.01 (0.22)	<0.081	<0.40	B2011
17112005-2727131	NIRSPEC	48.0	HD124897/K1.5 (G8-K5)	0.0027	3.79 (0.42)	<0.081	<0.21	B2011
17155573-2055312	NIRSPEC	21.2	HD19058/M4 (K2-M4)	0.0013	1.63 (0.18)	<0.91	<5.58	B2011
17160467-2057072	NIRSPEC	25.9	Gl268AB/M4.5 (M2-M4.5)	0.0027	2.13 (0.23)	<1.08	<5.07	B2011
17160860-2058142	NIRSPEC	19.6	Gl381/M2.5 (K1-M2.5)	0.0029	1.53 (0.17)	<0.69	<4.51	B2011
18140712-0708413*	NIRSPEC	15.1	HD9852/K0.5 (K0-K1)	0.0026	1.40(0.15)	<0.59	<4.21	B2011
18160600-0225539	NIRSPEC	10.0	HD216946/K5 (K1-K5)	0.0028	1.06 (0.19)	<0.71	<6.70	B2011
18165296-1801287	NIRSPEC	24.0	HD204724/M1 (K5-M3)	0.00094	1.62 (0.22)	<0.72	<4.44	B2011
18165917-1801158	NIRSPEC	26.7	HD94705/M5.5 (M2-M5.5)	0.00044	1.85 (0.20)	<0.96	<5.19	B2011
18170376-0815070	NIRSPEC	16.0	HD108849/M7 (M1-M7)	0.00052	0.99 (0.12)	<0.48	<4.85	
18170426-1802408	NIRSPEC	20.0	HD6903/F9 (F6-F9)	0.0014	1.09 (0.12)	<0.069	<0.63	B2011
18170429-1802540	NIRSPEC	23.7	HD28487/M3.5 (M1-M5.5)	0.00058	1.43 (0.20)	<0.069	<0.48	B2011
18170470-0814495	NIRSPEC	34.2	HD108849/M7 (M2-M7)	0.0014	3.93 (0.44)	2.77 (0.016)	7.05	B2011
18170957-0814136	NIRSPEC	26.2	HD39045/M3 (M3-M7)	0.00071	2.85 (0.31)	2.91 (0.015)	10.21	B2011
18171181-0814012	NIRSPEC	34.5	HD124897/K1.5 (K1.5-K2)	0.0012	3.81 (0.42)	5.37 (0.014)	14.10	B2011
18171366-0813188	NIRSPEC	28.6	HD76151/G2 (G2-M0)	0.0044	3.40 (0.38)	3.85 (0.49)	11.32	B2011
18171700-0813504	NIRSPEC	14.0	HD207076/M7 (M2-M7)	0.0023	0.68 (0.12)	<0.26	<3.82	
18172690-0438406	NIRSPEC	36.8	HD108849/M7 (M3-M7)	0.00084	4.31 (0.48)	3.48 (0.020)	8.07	B2011
18275901+0002337	IRTF	7.2	HD214665/M4 (M3-M4)	0.00043	<0.08	<0.23	...	
	NIRSPEC		HD194193/K7 (K4-M0)	0.00063		<0.083	...	
18282010+0029141	IRTF	10.6	HD94705/M5.5 (M2-M6)	0.00023	<0.17	<0.42	...	
	NIRSPEC		HD194193/K7 (K5-M3)	0.00059		<0.082	...	
18282631+0052133	IRTF	5.1	HD132935/K2 (G9-K2)	0.0012	<0.08	<0.16	...	
	NIRSPEC		HD2901/K2 (K1-K7)	0.00092		<0.044	...	
18284038+0044503	IRTF	12.5	HD214665/M4 (K3-M4)	0.0022	0.38 (0.13)	<0.47	<12.37	
	NIRSPEC		HD94705/M5.5 (K3-M5)	0.00060		<0.079	<2.08	
18284797+0037431	IRTF	10.6	HD214665/M4 (K5-M4)	0.00032	0.40 (0.08)	<0.32	<8.00	
	NIRSPEC		HD39801/M1-M2 (M0-M3)	0.00049		<0.073	<1.83	
18285266+0028242	NIRSPEC	36.0	HD28487/M3.5 (M3-M6)	0.0017	2.9 (0.2)	6.14 (0.48)	21.17	
18290316+0023090	IRTF	8.1	HD213893/M0 (M0-M5)	0.00030	0.23 (0.07)	<0.29	<12.61	
	NIRSPEC		HD194193/K7 (K4-M1)	0.00075		<0.060	<2.61	
18290436+0116207	IRTF	10.3	HD207991/K4 (K2-K4)	0.0035	0.18 (0.05)	<0.58	<32.22	
	NIRSPEC		HD187238/K3 (K2-M1)	0.0010		<0.040	<2.22	
18291619+0045143	NIRSPEC	6.1	HD124897/K1.5 (K1.5-K4)	0.00051	<0.10	<0.052	...	
18291699+0037191	IRTF	19.8	HD213893/M0 (M0-M4)	0.00084	1.06 (0.12)	<0.66	<6.23	
	NIRSPEC		HD95735/M2 (M0-M3)	0.0013		<0.071	<0.67	
18292528+0003141	IRTF	7.0	HD28487/M3.5 (M1-M3.5)	0.00022	<0.12	<0.15	...	
	NIRSPEC		HD39801/M1-M2 (K7-M3)	0.00061		<0.065	...	
18294108+0127449	IRTF	8.6	HD27598/M4 (K1.5-M4)	0.00023	<0.08	<0.066	...	
	NIRSPEC		HD91810/K1 (K1-K2)	0.00095		<0.066	...	
18300061+0115201	IRTF	46.0	HD236697/M0.5 (M0.5-M5.5)	0.010	3.04 (0.34)	<0.18	<0.59	
	NIRSPEC		HD108849/M7 (M3-M7)	0.00059		<0.090	<0.30	
	NIRSPEC		HD108849/M7 (M3-M7)	0.00059		<0.095	<0.31	B2011
18300085+0017069	IRTF	5.9	HD2901/K2 (G9-K2)	0.00040	<0.10	<0.17	...	
	NIRSPEC		HD132935/K2 (K0-K2)	0.0014		<0.035	...	
18300896+0114441	IRTF	13.1	HD207991/K4 (K4-M2)	0.00033	0.50 (0.17)	<0.32	<6.40	
	NIRSPEC		HD14469/M3-M4 (K2-M3)	0.00068		<0.063	<1.26	
19201597+1135146	NIRSPEC	25.1	HD39045/M3 (K5-M3)	0.00057	1.34 (0.14)	<0.87	<6.49	B2011
19201622+1136292	NIRSPEC	20.0	HD120477/K5.5 (K1.5-K5.5)	0.0013	1.01(0.11)	<0.062	<0.61	B2011
19214480+1121203	NIRSPEC	16.8	HD39045/M3 (M2-M3)	0.00063	1.43 (0.16)	<0.048	<0.34	B2011
21240517+4959100	NIRSPEC	24.8	HD28487/M3.5 (M0-M3.5)	0.00052	2.19 (0.24)	0.74 (0.21)	3.38	B2011
21240614+4958310	NIRSPEC	12.8	HD124897/K1.5 (K1.5-K3)	0.0011	0.98 (0.11)	<0.058	<0.59	B2011
22063773+5904520	NIRSPEC	13.9	HD10307/G1 (F5-G1)	0.0030	1.13 (0.12)	<0.044	<0.39	B2011

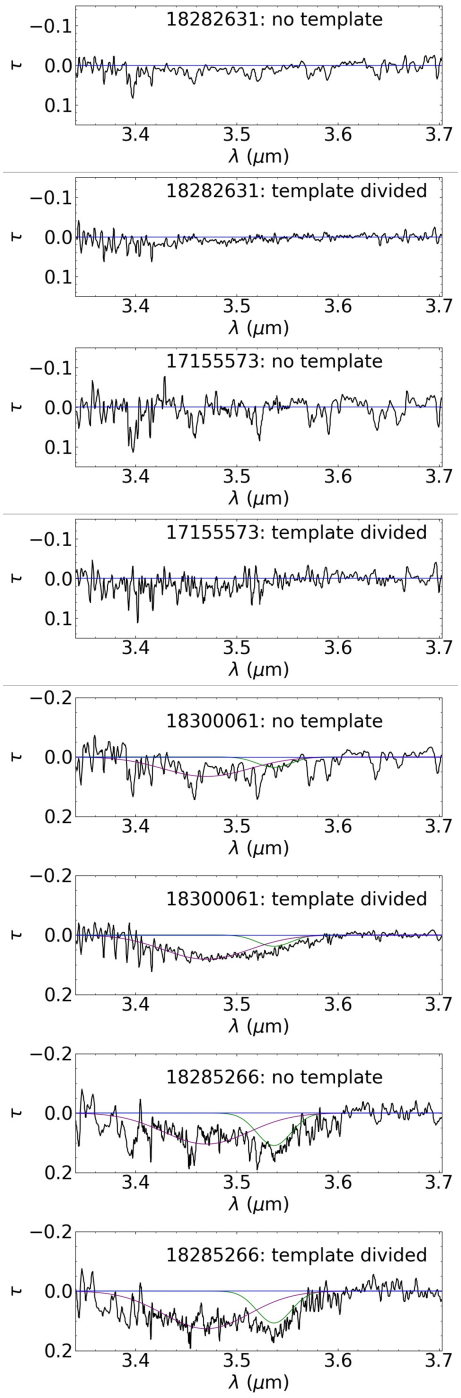

Figure 5.1: Optical depth spectra taken towards four background stars at varying visual extinctions: 2MASS J18282631 (A_V=5.1 mag), 2MASS J17155573 (A_V=10.6 mag), 2MASS J18300061 (A_V=46.0 mag), 2MASS J18285266 (A_V=36.0 mag). For each target, the two panels give the spectrum before (top) and after (bottom) template division, respectively. The blue line represents τ=0. The green and purple lines are Gaussian fits to the (tentative) 3.537 μm and 3.47 μm features, respectively.

corresponding reduced χ^2 values. The photosphere-corrected flux spectra and the final optical depth spectra are found in appendix 5.7.

To demonstrate the effect of the photospheric line correction, optical depth spectra with and without the correction are shown for four sources with A_V values in the range of 5.1-46.0 mag in Figure 5.1. Clearly, the reduction of photospheric lines allows for a more sensitive search for interstellar ice features. Blended photospheric lines could mimic narrow ice features, such as those of the CH_3OH band at 3.537 μm. Reduction of the photospheric lines also improves the fitting of the baseline. And for secure detections (e.g., 2MASS J18285266), a more reliable band profile is derived, as well as a more secure separation from the 3.47 μm feature.

When both the S/N and the photospheric line reduction are excellent, the CH_3OH ice abundance determination is limited by the decomposition of the 3.537 μm band from the broad ammonia hydrate feature at 3.47 μm. Unless a distinct dip at 3.537 μm is observed, the Gaussian decomposition (section 5.3) is uncertain.

For one of the targets in Boogert et al. (2011) we obtain different results. We do not confirm the CH_3OH ice detection toward 2MASS J18140712 ($7\pm2\times10^{16}$ cm^{-2} versus $< 6\times10^{16}$ cm^{-2} (3σ) in this work). Figure 5.2 shows that significant photospheric lines are still present after the division over the template. Perhaps our disagreement with Boogert et al. (2011) is due to the baseline choice.

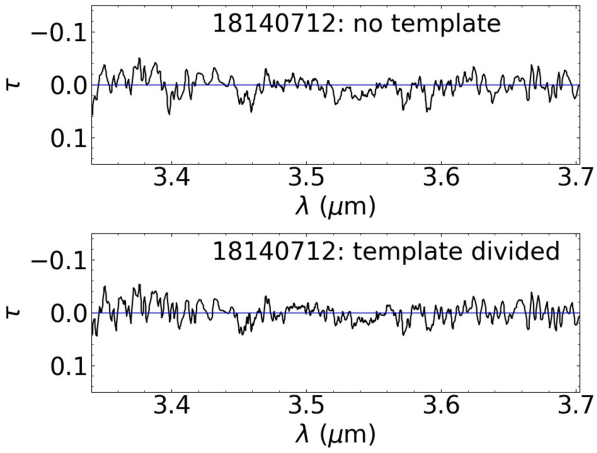

Figure 5.2: Optical depth spectra taken towards the field star, 18140712 (Boogert et al. 2011). No observable 3.537 μm CH_3OH feature is present in either panel, whereas the feature was present in Boogert et al. (2011). The choice of baseline may be the cause of such discrepancy. The blue line indicates τ=0.

5.4.1 CH_3OH column density relative to A_V and H_2O

Figure 5.3 shows the CH_3OH ice detections with 1σ error bars and 3σ upper limit values from Table 5.3 plotted as a function of the A_V. For upper limits of the same source, the lowest upper limit is plotted. Table 5.3 also shows the CH_3OH abundance relative to the H_2O ice column density. The A_V and N(H_2O)

values were taken from Boogert et al. (2011) and Boogert et al. (in preparation), and were determined by fitting observed 1-5 μm broad band photometry and spectra with a model consisting of spectra from the IRTF spectral database, the infrared interstellar extinction curve, an optical reddening of A_V/A_K = 8, and an H_2O ice spectrum for small spherical grains.

A fit is only made to the detections (closed blue circles). They apparently trace a distint environment particularly conducive to CH_3OH formation. As shown in the figure, the fit crosses the y-axis at A_V=13.5 ± 7.8 mag (i.e., the detection threshold). Taking into account the front and back of the cloud/core, the extinction as measured from the edge to the middle of the cloud/core along the line of sight is the observed value divided by 2, which results in a CH_3OH formation threshold of 6.8 ± 3.9 mag.

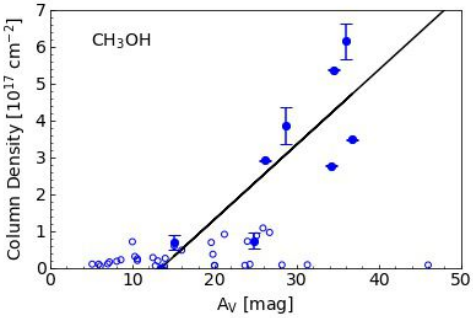

Figure 5.3: CH_3OH ice detections (solid blue circles; 1σ error bars) and upper limits (open blue circles; 3σ) plotted as a function of the visual extinction. A CH_3OH detection threshold of 13.5 ± 7.8 mag is found.

5.4.2 Averaging spectra in A_V bins

Spectra that do not show a secure CH_3OH feature at 3.537 μm are averaged into various A_V bins to increase the sensitivity (Figure 5.4). The averaging is weighed by $1/\sigma^2$, with σ the typical value used to determine the S/N column of Table 5.2. Three bins exist: an average over the lines of sight below the CH_3OH detection threshold, at and above the CH_3OH detection threshold, and with CH_3OH detections. The noise level in the $A_V < 18$ mag bin is 0.16, with a 3σ upper limit of 7.68×10^{17} cm^{-2} for the 3.537 μm feature. For the $A_V \geqslant 18$ mag bin, the noise level is 0.15, with a 3σ upper limit of 5.26×10^{16} cm^{-2} for the 3.537 μm feature. A noise level of 0.056 and a CH_3OH column density of 2.58×10^{18} cm^{-2} are measured for the bin containing CH_3OH detections. The A_V range of < 18 mag in Figure 5.4 does not show any observable CH_3OH feature. The 3.47 μm $NH_3{\cdot}H_2O$ feature is clearly present at $A_V \geqslant 18$ mag, however there is no distinct feature at 3.537 μm.

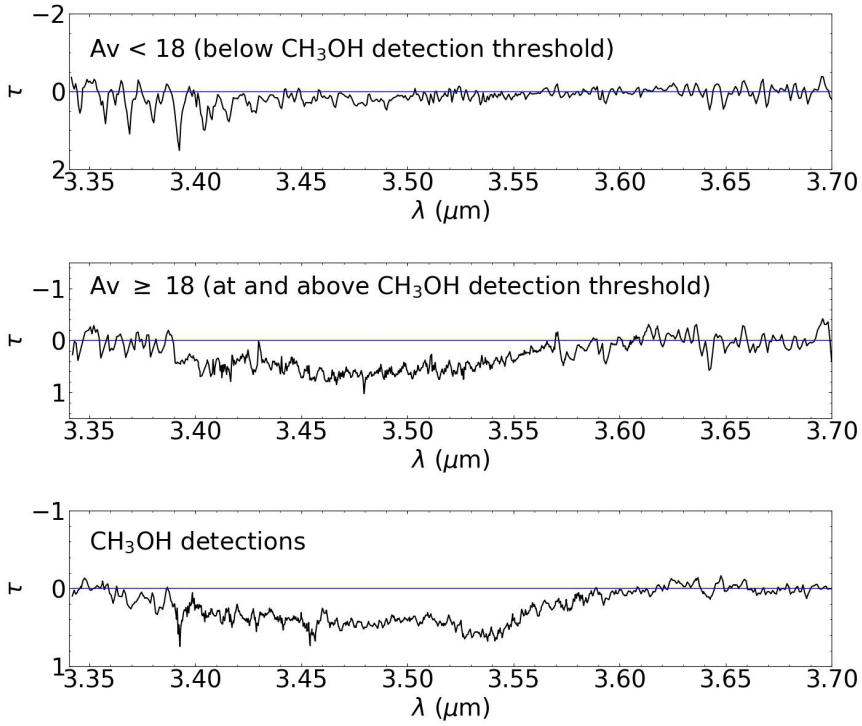

Figure 5.4: Optical depth spectra averaged across the indicated A_V bins, for targets without a CH_3OH ice detection, as probed by the 3.537 μm feature (see Table 5.3). For reference, a spectrum averaged over sight-lines with CH_3OH detections is shown in the bottom panel. The blue line shows τ=0. The number of targets in each bin is 30, 18, and 7 for $A_V < 18$, $A_V \geqslant 18$, and CH_3OH detections averaged, respectively. Note that the detection for sight-line 2MASS J18140712 is not included.

5.5 Discussion

The extinction threshold for ice formation is a direct observational indicator of the chemical evolution of molecular clouds. The observed A_V values mentioned above sample both, the front and back of the clouds/cores. And thus, the maximum depth into the clouds/cores that is traced by these observations is $A_V/2$ (i.e., the formation threshold), which we will use in the remainder of this discussion.

The threshold value for abundant CH_3OH formation of A_V=6.8 ± 3.9 mag as derived from the linear fit is of low significance (1.7σ), reflecting the large spread in the CH_3OH abundances, while the uncertainties on the individual abundances are small.

Also, for many high extinction sight-lines, tight CH_3OH abundance upper limits were derived (Table 5.3), well below the detections at similar A_V (Figure 5.3). This strengthens the trend observed in Boogert et al. (2015). We speculate that CO has not sufficiently frozen out in these sight-lines, limiting the CH_3OH formation in some of these dense clouds and dark cores. CO

freeze out could have been suppressed by lower densities at the same A_V, by higher dust temperatures or radiation fields. Alternatively, CH_3OH may have been consumed or destroyed. Other formation channels that overlap with the CH_3OH formation route, such as those of HCOOH (Qasim et al. 2019a), may also be contributing factors.

Below A_V=7.6 mag, only upper limits are available, but they are tight (<0.39% H_2O), supporting that the threshold for abundant CH_3OH formation is indeed well above that for H_2O (~ 1.6) and CO (~ 3). CH_3OH formation below these limits is expected, however. As reported in the laboratory investigations by Bergner et al. (2017) and Qasim et al. (2018), CH_4 is a precursor to CH_3OH formation under low temperature molecular cloud conditions. The formation efficiency is a factor of ~20 below that of the high density CO ice hydrogenation route (Qasim et al. 2018). CH_4 is formed at low extinctions (A_V ~ 2 mag), similar to H_2O. At this stage, CO formation in the gas phase is not complete, and could enhance the CH_4 abundance in the first grain mantle layers. There is indeed a hint of enhanced CH_4 ice abundances at low extinctions (Öberg et al. 2008). Consequently, CH_3OH is expected to be present in the ices well below the threshold for enhanced formation via the CO ice hydrogenation route discussed above.

5.6 Conclusions and future work

Observations targeting the 3.537 μm feature of CH_3OH ice in dense molecular clouds and dark cores to constrain the CH_3OH ice formation threshold were pursued. A method to increase the sensitivity to weak ice absorption features and thus to the accuracy of the CH_3OH column density is presented. The following conclusions can be drawn from this work:

1) The method of fitting template spectra of unreddended stars to reduce photospheric lines from dense cloud and dark core background spectra increases the sensitivity to detect ice features. It also improves the accuracy of the baseline determination. With respect to the study of (Boogert et al. 2011), one new CH_3OH ice detection was made and one was not found. The total number of CH_3OH ice detections in quiescent molecular cloud and core material is now 8.

2) This photospheric correction method will be applicable to the analysis of future JWST spectra. Multi-object spectroscopy with JWST will make it possible to observe large sample sizes for both, background and template stars.

3) For high S/N spectra that are well corrected for photospheric lines, the limiting factor for accurate CH_3OH ice abundances is the decomposition of the 3.537 μm band from the 3.47 μm band of ammonia hydrates.

4) The CH_3OH formation threshold is constrained to be A_V=6.8 ± 3.9 mag. The error bars on the individual measurements are much smaller than the scatter in the column densities. No detections have been made below a formation threshold of A_V=7.6 mag. The abundance upper limits obtained in many sightlines both below and above the 13.5 mag detection threshold are significant.

6) The large scatter at high A_V values is puzzling. Perhaps CO is not an abundant resource for CH_3OH formation in some of these clouds and cores. Alternatively, CH_3OH may have been effectively destroyed.

7) The threshold for the efficient formation of CH_3OH via the CO ice hydrogenation route does not preclude the formation via less efficient pathways. Such pathways may well include CH_4 and/or CH_4 precursors (C, CH, etc.), as supported from recent laboratory experiments.

8) The sample size of CH_3OH detections is small and more observations are warranted to further investigate the origin of the large scatter in the CH_3OH abundance variations as well as the formation threshold.

9) Tracing the columns of CO and CH_4 alongside CH_3OH in the same clouds and cores will help understand how and when CH_3OH is formed. Whether CO is actually depleted in regions where CH_3OH is not detected, and if CH_4 could be a precursor for less abundant CH_3OH, can be better understood by mapping these ices simultaneously. JWST is ideally suited for this, because of its large wavelength coverage, high sensitivity, and mapping capabilities.

5.7 Appendix information

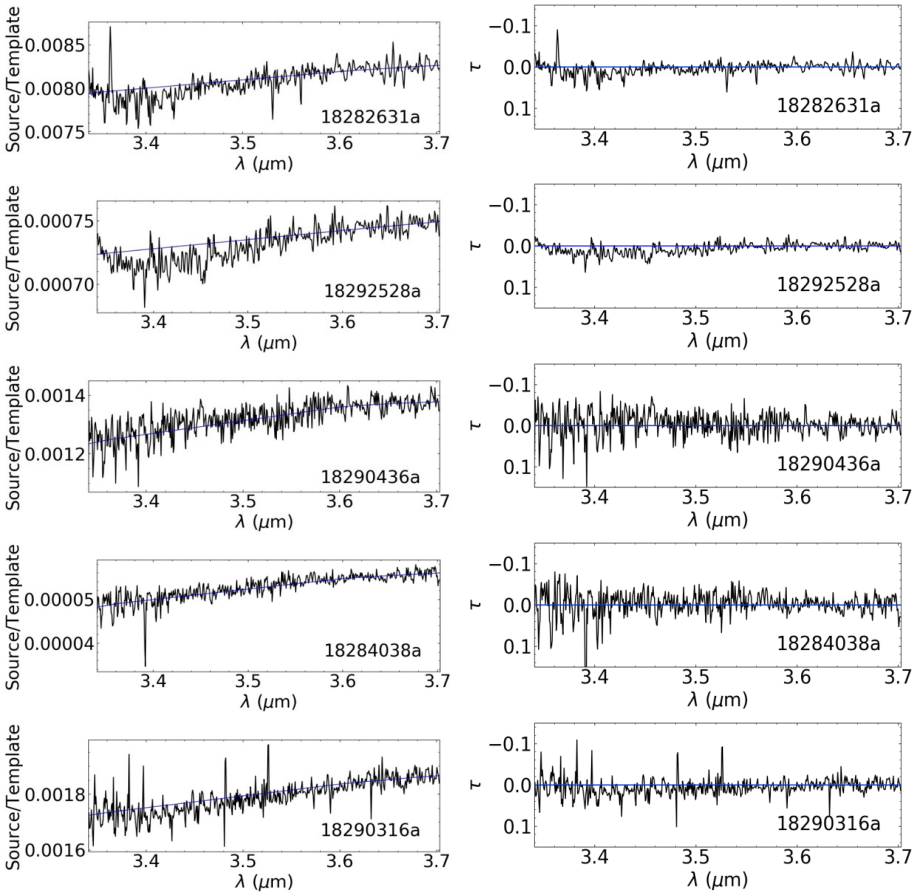

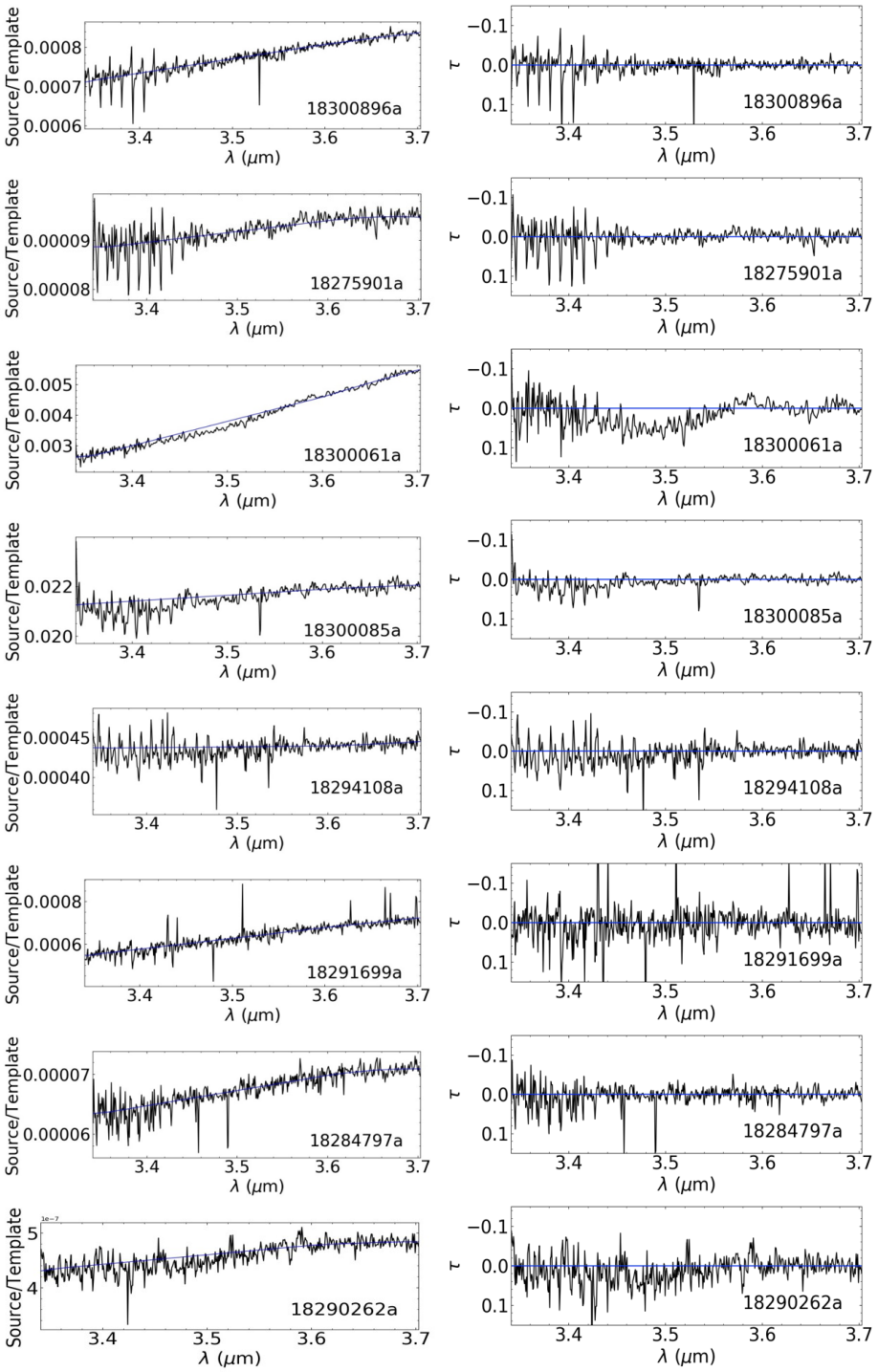
Source/Template
τ
λ (μm)
18300896a
18275901a
18300061a
18300085a
18294108a
18291699a
18284797a
18290262a

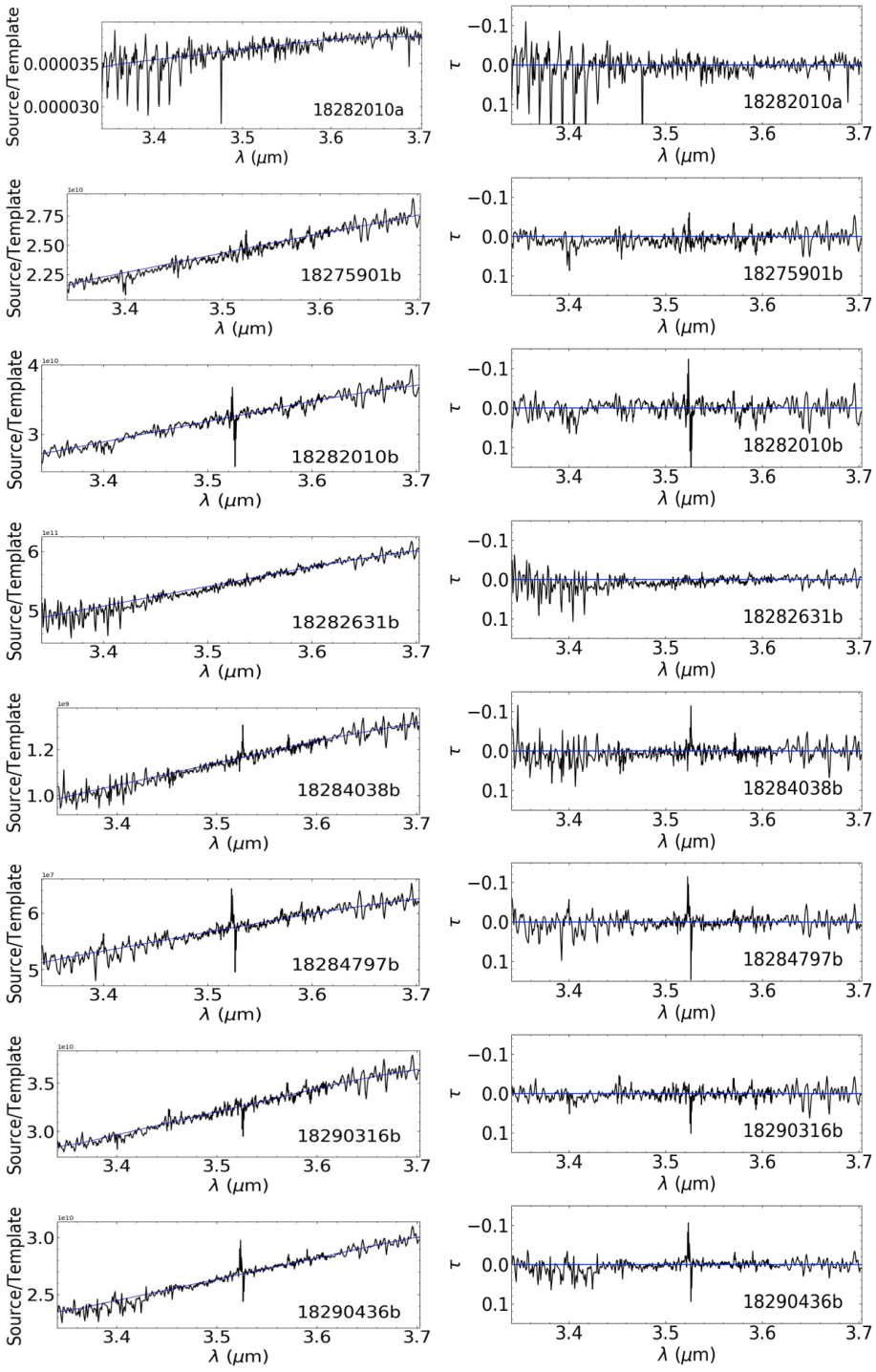
Source/Template
τ
λ (μm)
18282010a
18275901b
18282010b
18282631b
18284038b
18284797b
18290316b
18290436b

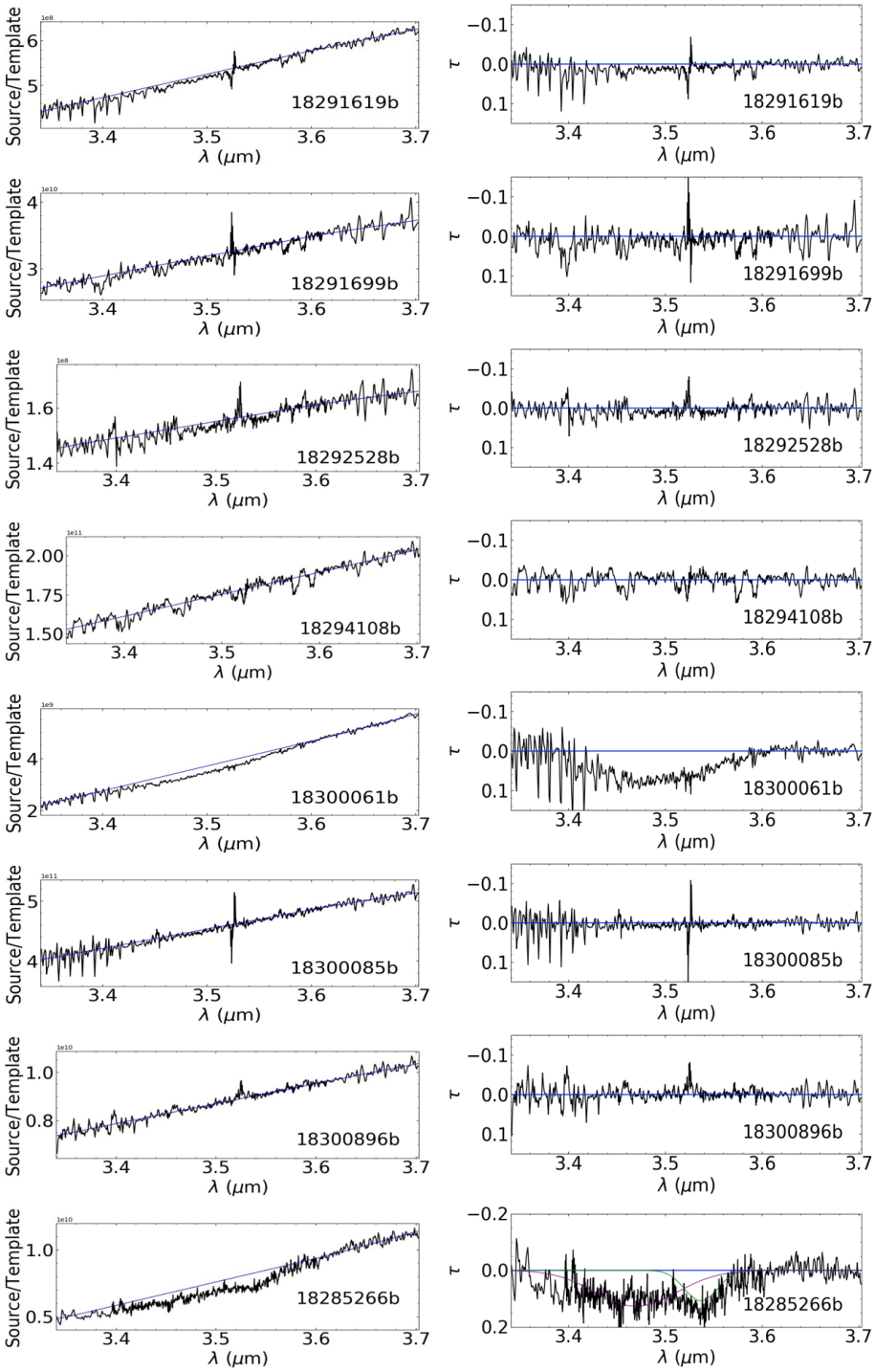
Source/Template
λ (μm)
18291619b
τ
18291619b
18291699b
18291699b
18292528b
18292528b
18294108b
18294108b
18300061b
18300061b
18300085b
18300085b
18300896b
18300896b
18285266b
18285266b

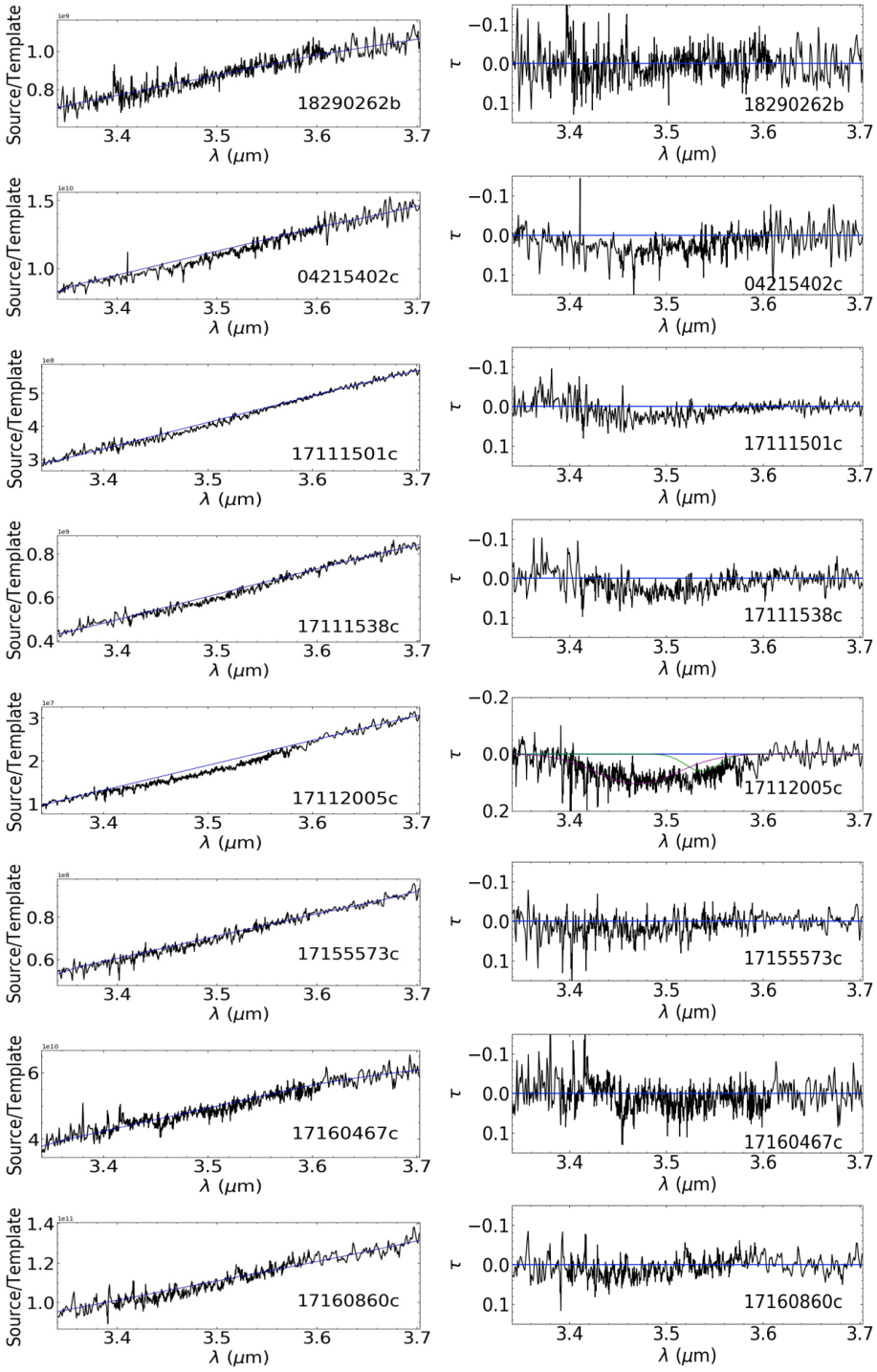
Source/Template
τ
λ (μm)
18290262b
04215402c
17111501c
17111538c
17112005c
17155573c
17160467c
17160860c

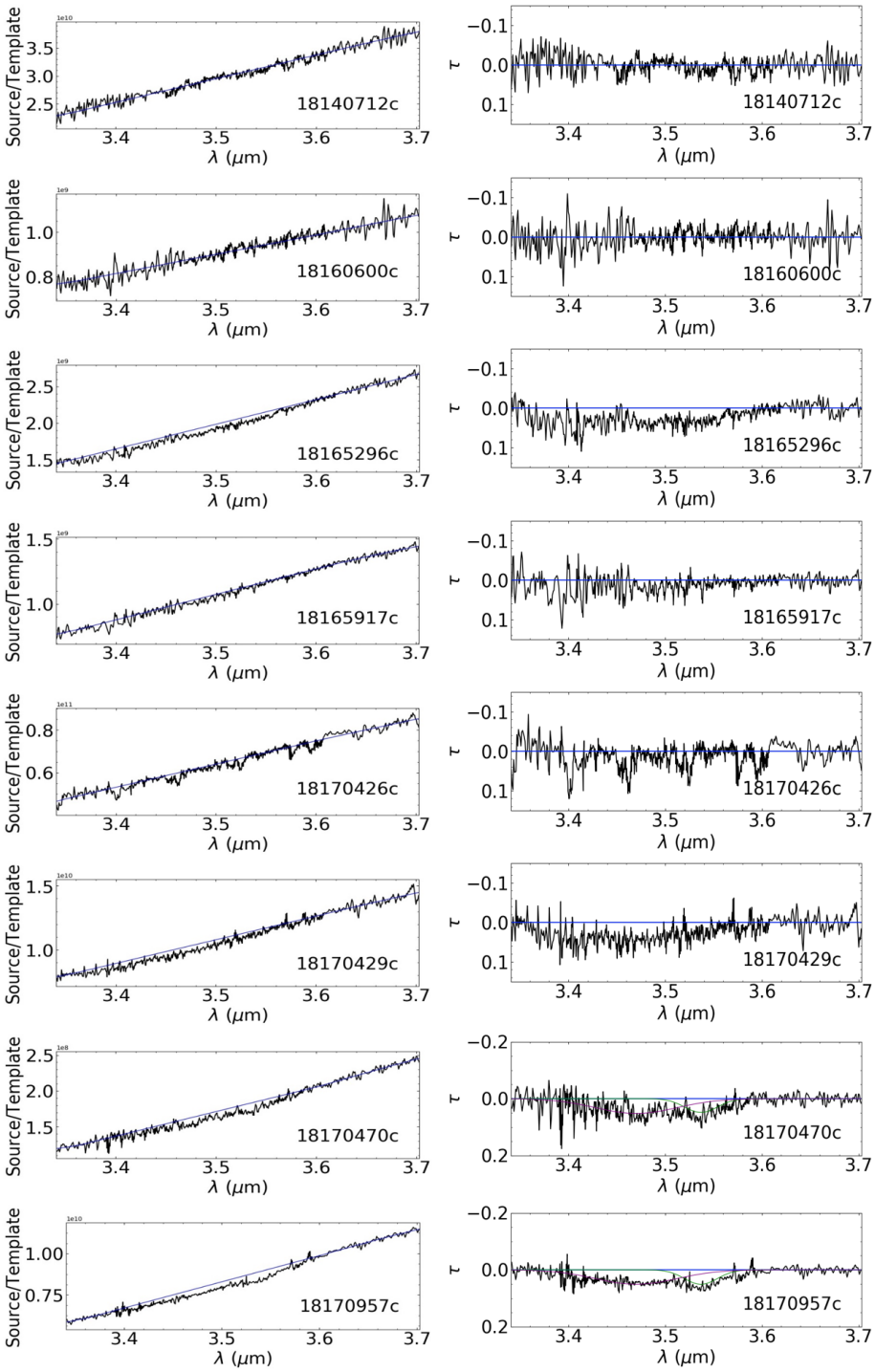
Source/Template
τ
λ (μm)
18140712c
18160600c
18165296c
18165917c
18170426c
18170429c
18170470c
18170957c

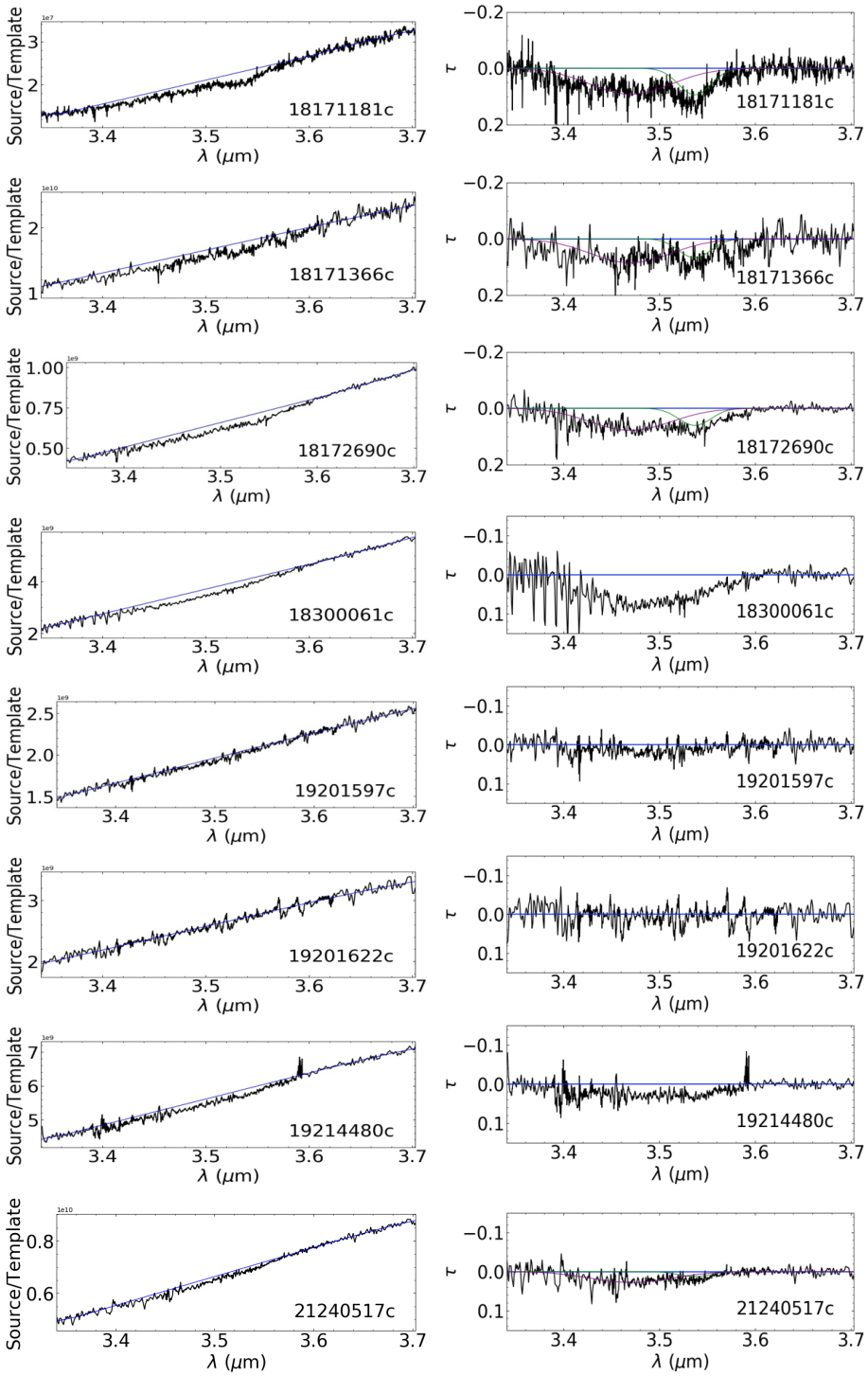
Source/Template
λ (μm)
18171181c
τ
18171366c
18172690c
18300061c
19201597c
19201622c
19214480c
21240517c

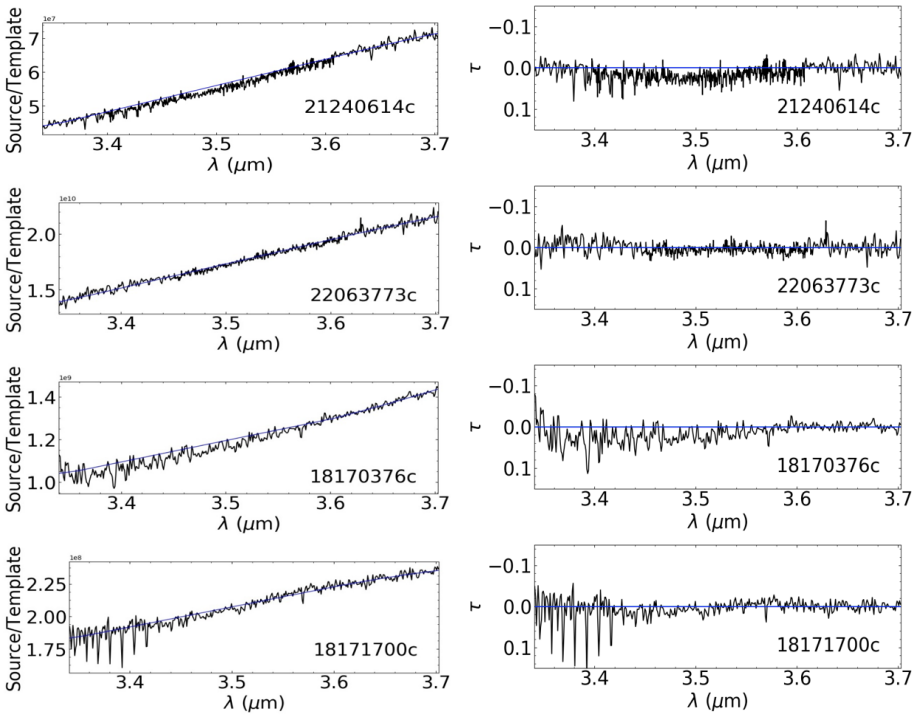

Figure 5.5: Flux and optical depth spectra of the 3.3-3.7 μm wavelength ragion towards the entire sample. The blue line in each left panel is the local continuum, and in the right panel is τ=0. The green and purple lines are Gaussian fits for the 3.537 μm and 3.47 μm absorption features, respectively.

Bibliography

Bergner, J. B., Öberg, K. I., & Rajappan, M. 2017, Astrophys. J., 845, 29
Boogert, A., Gerakines, P. A., & Whittet, D. C. 2015, Annu. Rev. Astron. Astrophys., 53, 541
Boogert, A., Huard, T., Cook, A., et al. 2011, Astrophys. J., 729, 1
Brooke, T., Sellgren, K., & Geballe, T. 1999, Astrophys. J., 517, 883
Cardelli, J. A., Clayton, G. C., & Mathis, J. S. 1989, Astrophys. J., 345, 245
Charnley, S., Tielens, A., & Millar, T. 1992, Astrophys. J., 399, L71
Chiar, J., Adamson, A., Kerr, T., & Whittet, D. 1995, Astrophys. J., 455, 234
Chiar, J., Pendleton, Y., Allamandola, L., et al. 2011, Astrophys. J., 731, 9
Chuang, K.-J., Fedoseev, G., Ioppolo, S., van Dishoeck, E. F., & Linnartz, H. 2016, Mon. Not. R. Astron. Soc., 455, 1702
Cuppen, H., van Dishoeck, E. F., Herbst, E., & Tielens, A. 2009, Astron. Astrophys., 508, 275
Cushing, M., Vacca, W., & Rayner, J. 2004, Publ. Astron. Soc. Pac., 116, 362
Dartois, E., & d'Hendecourt, L. 2001, Astron. Astrophys., 365, 144
Fedoseev, G., Chuang, K.-J., Ioppolo, S., et al. 2017, Astrophys. J., 842, 1
Fuchs, G., Cuppen, H., Ioppolo, S., et al. 2009, Astron. Astrophys., 505, 629
Goumans, T., & Kästner, J. 2011, J. Phys. Chem. A, 115, 10767

Jørgensen, J., Schöier, F., & van Dishoeck, E. F. 2005, Astron. Astrophys., 435, 177
Kerkhof, O., Schutte, W., Ehrenfreund, P., et al. 1999, Astron. Astrophys., 346, 990
McLean, I. S., Becklin, E. E., Bendiksen, O., et al. 1998, 3354, 566
Öberg, K. I., Boogert, A., Pontoppidan, K. M., et al. 2008, Astrophys. J., 678, 1032
Öberg, K. I., Garrod, R. T., van Dishoeck, E. F., & Linnartz, H. 2009, Astron. Astrophys., 504, 891
Pontoppidan, K. M. 2006, Astron. Astrophys., 453, L47
Pontoppidan, K. M., Dartois, E., van Dishoeck, E. F., Thi, W.-F., & d'Hendecourt, L. 2003, Astron. Astrophys., 404, L17
Qasim, D., Chuang, K.-J., Fedoseev, G., et al. 2018, Astron. Astrophys., 612, 1
Qasim, D., Lamberts, T., He, J., et al. 2019a, Astron. Astrophys., 626, A118
Qasim, D., Fedoseev, G., Chuang, K.-J., et al. 2019b, Astron. Astrophys., 627, A1
Rayner, J., Cushing, M., & Vacca, W. 2009, Astrophys. J. Suppl. Ser., 185, 289
Rayner, J., Toomey, D., Onaka, P., et al. 2003, Publ. Astron. Soc. Pac., 115, 362
Shimonishi, T., Dartois, E., Onaka, T., & Boulanger, F. 2016, Astron. Astrophys., 585, A107
Soma, T., Sakai, N., Watanabe, Y., & Yamamoto, S. 2018, Astrophys. J., 854, 116
Vacca, W., Cushing, M., & Rayner, J. 2003, Publ. Astron. Soc. Pac., 115, 389
van Dishoeck, E. F., Blake, G. A., Draine, B. T., & Lunine, J. 1993, in Protostars and Planets III, 163–241
Watanabe, N., & Kouchi, A. 2002, Astrophys. J. Lett., 571, L173
Wirström, E., Geppert, W. D., Hjalmarson, Å., et al. 2011, Astron. Astrophys., 533, A24